

Structural phase transitions of the metal oxide perovskites SrTiO₃, LaAlO₃, and LaTiO₃ studied with a screened hybrid functional

Fedwa El-Mellouhi,^{1,*} Edward N. Brothers,^{1,†} Melissa J. Lucero,² Ireneusz W. Bulik,² and Gustavo E. Scuseria^{2,3,4}

¹*Department of Chemistry, Texas A&M at Qatar, Texas A&M Engineering Building, Education City, Doha, Qatar*

²*Department of Chemistry, Rice University, Houston, Texas 77005-1892, USA*

³*Department of Physics and Astronomy, Rice University, Houston, Texas 77005-1892, USA*

⁴*Chemistry Department, Faculty of Science, King Abdulaziz University, Jeddah 21589, Saudi Arabia*

(Received 22 April 2012; revised manuscript received 30 October 2012; published 4 January 2013)

We have investigated the structural phase transitions of the transition metal oxide perovskites SrTiO₃, LaAlO₃, and LaTiO₃ using the screened hybrid density functional of Heyd, Scuseria, and Ernzerhof (HSE06). We show that HSE06-computed lattice parameters, octahedral tilts, and rotations, as well as electronic properties, are significantly improved over semilocal functionals. We predict the crystal-field splitting (Δ_{CF}) resulting from the structural phase transition in SrTiO₃ and LaAlO₃ to be 3 meV and 10 meV, respectively, in excellent agreement with experimental results. HSE06 identifies correctly LaTiO₃ in the magnetic states as a Mott insulator. Also, it predicts that the GdFeO₃-type distortion in nonmagnetic LaTiO₃ will induce a large Δ_{CF} of 410 meV. This large crystal-field splitting associated with the large magnetic moment found in the G-type antiferromagnetic state suggests that LaTiO₃ has an induced orbital order, which is confirmed by the visualization of the highest occupied orbitals. These results strongly indicate that HSE06 is capable of efficiently and accurately modeling perovskite oxides and promises to efficiently capture the physics at their heterointerfaces.

DOI: [10.1103/PhysRevB.87.035107](https://doi.org/10.1103/PhysRevB.87.035107)

PACS number(s): 71.15.Mb, 71.15.Ap, 77.80.B-, 77.84.-s

I. INTRODUCTION

Heterointerfaces between metal oxides such as SrTiO₃ (STO), LaAlO₃ (LAO), and LaTiO₃ (LTO) show considerable promise as components in all-oxide electronics because they exhibit unique properties unobserved in the corresponding isolated parent compounds. In their bulk phase, SrTiO₃ and LaAlO₃ are nonmagnetic wide-band-gap materials, but when assembled into superlattices, interesting properties such as high- T_c superconductivity, magnetism, ferroelectricity, and colossal magnetoresistance are observed. Despite recent experimental and theoretical activities, the field of oxide interfaces remains full of surprises and unsolved problems.^{1,2}

A number of heterointerface behaviors have been explained using density functional theory (DFT), but several authors (see Refs. 3 and 4 and references therein) have shown that more elaborate methods such as dynamical mean field theory⁵⁻⁷ or *GW*-based approaches⁸ are needed to successfully model interfaces of strongly correlated electronic systems and predict the direction of charge transfer. While many-body techniques in combination with DFT methods are sufficient for this task, they remain computationally demanding, particularly when it is necessary to account for the important structural relaxations and phase transitions occurring at interfaces.

Theory's predictive power can be enhanced by considering the properties of the two (or more) parent materials in the bulk phase, followed by mapping to obtain heterointerface properties.^{9,10} To successfully model the perovskites considered herein, good band gaps and accurate structural/geometric properties beyond reasonable lattice parameters are required. For example, the TiO₆ rotation and tilt angles are likely responsible for the metal-insulator transition in oxide superlattices¹¹ and necessitate accurate theoretical structures.

Controlling the octahedral rotations relies on good geometric values of TiO₆ and is considered by some to be the key to designing functional metal oxides.¹² Further, the TiO₆ rotation

and/or tilts affect the electronic properties of both bulk metal oxides and their superlattices. For example, the degeneracy of the t_{2g} states in (LAO)₅/(LTO)_{*n*}/(LAO)₅ superlattices is lifted by the crystal field induced by the TiO₆ octahedral rotation in the LaTiO₃ layer.¹³ Consequently, accurate determination of crystal-field splittings (CFS) induced by the phase transition in bulk metal oxides is also important to the Ti-3*d* orbital reconstruction at the heterointerfaces.¹⁴

Recently, Jalan *et al.*¹⁵ found that stress also exerts a pronounced influence on the electron mobility in STO, with moderate strains resulting in a greater than 300% increased mobilities. Good theoretical estimation of strain in metal oxides is thus recommended and computational methods approaching the experimental strain are preferred. This is the case for the recent HSE06 calculations of Janotti *et al.*,¹⁶ which confirmed the experimental findings and showed that strain in STO affects seriously the electronic effective masses and the conductivity.

A survey of the literature (see Ref. 17 and references therein) presented in Table I below summarizes the main semilocal and hybrid functional trends for bulk SrTiO₃, a widely used substrate for the heterointerface superlattices of interest here. Methods underestimating the band gaps, such as the local spin density approximation¹⁸ (LSDA), the generalized gradient approximation functional of Perdew, Burke, and Ernzerhof^{19,20} (PBE), and the PBEsol^{21,22} reparameterization for solids, must be avoided because they lead to an overestimation of the two-dimensional band at the heterointerfaces and tend to overestimate the octahedral rotation angle in SrTiO₃. In addition, LSDA and PBE also fail to describe the antiferromagnetic insulating character in strongly correlated systems.

DFT + *U* methods can open the band gap to the experimental value by empirical tuning of the value of the Coulomb on-site (*U*) and exchange (*J*) interaction parameters, but at the cost of incorporating parameters that are external to theory and

TABLE I. Trends observed in the performance of DFT and post-DFT calculations applied to bulk SrTiO₃ regardless of the basis sets used (see Ref. 17). Hybrids account for both global [B3PW (Refs. 24–26), B3LYP (Ref. 26), and B1-WC (Ref. 27)] and screened (HSE and HISS) hybrid functionals.

Functional	LSDA	PBEsol	PBE	DFT + U	Hybrids
Lattice parameter	Too low	Good	Too big	Too low	Good
Band gaps	Too small –40%	Too small –40%	Too small –40%	Good	Good ±6%
TiO ₆ rotation angle	Too big Up to 8°	Too big 5°	Too big 4°	Too big 4°–5°	Good 1°–2°

are material dependent. While DFT + U can correctly describe the insulating character of LaTiO₃ in the ground state,²⁸ geometric issues such as the rotation angle overestimation problems in STO, which originate from the parent functionals LSDA and PBE, do not improve by adding the + U correction. Despite these well-known limitations, DFT + U has been the method of choice for the oxide superlattice calculations, mainly because the corrected gaps approach the experimental band gaps of SrTiO₃, LaAlO₃, and LaTiO₃ bulk phases with a minimal additional cost compared to regular DFT calculations, especially for superlattices.^{29,30}

Very important progress has been made in furthering our understanding of metal oxide superlattices using DFT + U ; however, one value of U will not produce the correct band gap for differing bulk metal oxides, which poses a problem for heterostructure systems such as LAO/STO, LTO/STO, and LTO/LAO. In fact, most DFT + U calculations assume that the value of U appropriate for the substrate is also valid to describe the grown material, as well as the heterointerface,^{11,28,31} although in some instances the U correction is applied to the bulk only, while the grown material is treated at the regular DFT level.³² (Even more sophisticated methods use different values of U and J for the Ti-3 d and La-4 f states; see for example Ref. 33.) Another problem recently gaining notoriety is the fact that DFT + U predicts exaggerated octahedral distortions in the fully relaxed superlattices,³³ which seriously affects the electronic structure and the properties of the 2D electron gas at the interfaces. All of these shortcomings indicate the need for a universally applicable functional to better describe the electronic structure of thin films and their interfaces.

Electronic structure calculations on bulk SrTiO₃ using the global hybrid functionals B3PW,³⁴ B3LYP,^{35,36} and B1-WC³⁷ were performed by several groups,^{24,25,38} showing improved band gaps compared to semilocal DFT. For example, band gap deviations from experiment were only 6%–7% with B3PW, while structural properties and order parameters of the antiferrodistortive (AFD) phase (see Table I) were also closer to experiment. Nevertheless, the use of global hybrids in studying heterointerfaces remains limited due to their high computational cost.

Screened hybrid density functionals such as that of Heyd, Scuseria, and Ernzerhof³⁹ (HSE/HSE06) and the middle-range screened hybrid functional of Henderson, Izmaylov, Scuseria, and Savin (HISS)⁴⁰ are excellent candidates for this task due to their accuracy and much lower computational cost compared to regular hybrids.^{41–44} Screened hybrid functionals yield SrTiO₃ structural properties for both phases^{17,45} in very good agreement with experiment,⁴⁶ especially if used with

large (but still computationally tractable) basis sets. The best results arise from the HSE/TZVP combination.¹⁷

Previous calculations on iron⁴⁷ and transition metal monoxides⁴⁸ using HSE03⁴⁹ indicate that the magnetic moment, exchange splitting, and bandwidth in metals are overestimated relative to experiment. Subsequent tests on strongly correlated magnetic materials have been carried out by Rivero *et al.*²³ using the short-range screened hybrid HSE06 and the long-range screened hybrid LC- ω PBE.⁵⁰ They demonstrated that both range-separated hybrids give a good quantitative description of the electronic structure of strongly correlated systems, with magnetic coupling constants that are larger than experiment, yet improved compared to the results of the global hybrid, B3LYP.

A more recent work from Philipps and Peralta⁵¹ involving transition metal molecular complexes suggests that HSE06 is a promising alternative for the evaluation of exchange couplings in extended systems, again because of reasonable accuracy at reduced computational expense. The present paper is a continuation of earlier work¹⁷ with SrTiO₃; herein, we assess the accuracy of HSE06 for calculating the crystal-field splitting in SrTiO₃, the geometries of LaAlO₃ in its different phases, as well as the structural and magnetic properties of the strongly correlated system, LaTiO₃.

II. COMPUTATIONAL METHODS

All calculations presented in this paper were performed using a development version of the GAUSSIAN suite of programs,⁵² with the periodic boundary condition (PBC)⁵³ code used throughout. Unless otherwise noted, crystal structures were downloaded as CIF files from the ICSD.⁵⁴ (See Ref. 54 for the specific ID numbers.)

The Def2-⁵⁵ series of GAUSSIAN basis sets were optimized for use in bulk LaTiO₃ and LaAlO₃ calculations, following the procedure described in Ref. 17 for bulk SrTiO₃. We use the notation TZVP and SZVP to differentiate these optimized PBC basis sets from the molecular Def2-TZVP and Def2-SZVP basis sets. The functionals applied in this work include the LSDA¹⁸ (SVWN5),⁵⁶ PBE, and HSE06. LSDA and PBE calculations were utilized to assess the quality of the GAUSSIAN basis sets via comparison with plane wave calculations from the literature.

Most numerical settings in GAUSSIAN were left at the default values, e.g., geometry optimization settings, integral cutoffs, k -point meshes, and SCF convergence thresholds. For LaAlO₃, the reciprocal space integration used a 12 × 12 × 12 k -point mesh for the cubic unit cells of 5 atoms, while for the larger

rhombohedral supercell of 30 atoms, the default k -point mesh of $8 \times 8 \times 4$ was found to be sufficient. Because we performed optimizations of both atomic positions and lattice parameters, the SCF convergence threshold was set to TIGHT, or 10^{-8} atomic units. The fully relaxed structures can be obtained from the Cambridge Structural Database.⁵⁷

Due to the metallic nature of LaTiO_3 , a mesh of $24 \times 24 \times 18$ for the k -point sampling was required in order to ensure stable convergence.⁴⁷ For the sake of computational efficiency, all calculations on LTO were carried out using the SZVP basis set.

III. RESULTS AND DISCUSSION

A. SrTiO_3

Under ambient conditions, bulk SrTiO_3 crystallizes in a cubic perovskite structure, subsequently undergoing a second-order phase transition at $T_c = 105$ K to a tetragonal structure with slightly rotated oxygens around the z axis, known as the antiferrodistortive (AFD) phase. The phase transition of STO is governed by two order parameters. The primary order parameter is the rotation angle of the TiO_6 octahedra (θ) that can reach up to 2.1° at 4.2 K.⁵⁸ The second order parameter measures the tetragonality of the unit cell, as defined by the ratio of c/a , and can be as large as 1.0009 upon cooling to 10 K.⁵⁹

The finer details of the conduction band splitting induced by the AFD phase transition in STO are still under debate,⁶⁰⁻⁶³ with discrepancies between theory and experiment arising from differences in the sample dopant or defect concentrations: The TiO_6 rotation angle may be enhanced or reduced depending on the doping conditions and this affects directly the rotation of oxygen atoms in the xy plane when STO distorts into the AFD phase.

We have shown¹⁷ in modeling an idealized STO (with no defects, doping, strain, or surface effects) that HSE06 provides band gaps and phase transition order parameters in excellent agreement with experiment. We found a $c/a = 1.0012$ corresponding to a $+0.12\%$ tensile strain along the [001] direction or the z axis. However, we did not address the crystal-field splitting (Δ_{CF}) of the conduction band minimum (CBM) induced by the phase transition. As is evident from the enlargement of the region around the calculated CBM at the Γ point the crystal field causes the threefold degenerate band to

split into a doubly degenerate band and a single band 3 meV higher in energy.

Further discussion arises from Fig. 1 by zooming at 10% from the Brillouin zone center along the high-symmetry [100] (D), [001] (Δ), [101] (S), (S), [110] (Σ), and [111] (Λ), in the body-centered tetragonal Brillouin zone. Along Δ , D , and S , we observe a qualitative behavior very similar to that predicted in an earlier augmented plane wave (APW) calculation without spin-orbit (SO) coupling.⁶³ However, differences arise along Σ and Λ directions where we observe that the lowest doubly degenerate band splits into a heavy-electron and a light-electron band as we move farther from the Γ point. The differences might come from the model used in the APW calculation by Mattheiss neglecting both the nearest and second-nearest neighbor oxygen-oxygen $2p$ interactions and the interaction between the oxygen- $2s$ and the titanium- t_{2g} orbitals in the cubic state.

Quantitatively, the APW calculations predict $\Delta_{\text{CF}}^{\text{APW}} = 20.7$ meV which is much greater than the $\Delta_{\text{CF}}^{\text{HSE06}} = 3$ meV we obtain in the present work. This is also the case for the spin-orbit splitting for cubic STO $\Delta_{\text{SO}}^{\text{APW}} = 83$ meV, if compared with $\Delta_{\text{SO}}^{\text{HSE06}} = 28$ meV computed using the VASP plane wave code by Janotti *et al.*¹⁶

Janotti *et al.* studied with HSE06 the effect of $\pm 1\%$ strain on the CBM focusing on the splittings and the electron effective masses taking into account the spin-orbit effects. They also found that the rotation of TiO_6 octahedra around the z axis without including the tetragonal distortion ($c > a$) leads to a splitting of the doubly degenerate band of 4 meV with minor changes on the effective masses. Going back to our results in Fig. 1, one concludes that the small $+0.12\%$ tensile strain along the [001] direction arising from the tetragonal distortion might not contribute significantly to the CBM splitting but plays a role in the important differences in the electron effective masses we observe along the high-symmetry directions. For example, the curvature of the CBM is higher (i.e., lower effective mass or light electrons) along S and Δ directions—parallel to the strain—indicating higher electron mobilities in those directions. This result is in line with the enhanced electron mobility Janotti *et al.* concluded for SrTiO_3 subject to $+1\%$ tensile strains along the (001) direction. However, further investigation is still needed to draw a final conclusion since the electron effective masses and the order of the bands change upon the inclusion of SO effects.¹⁶

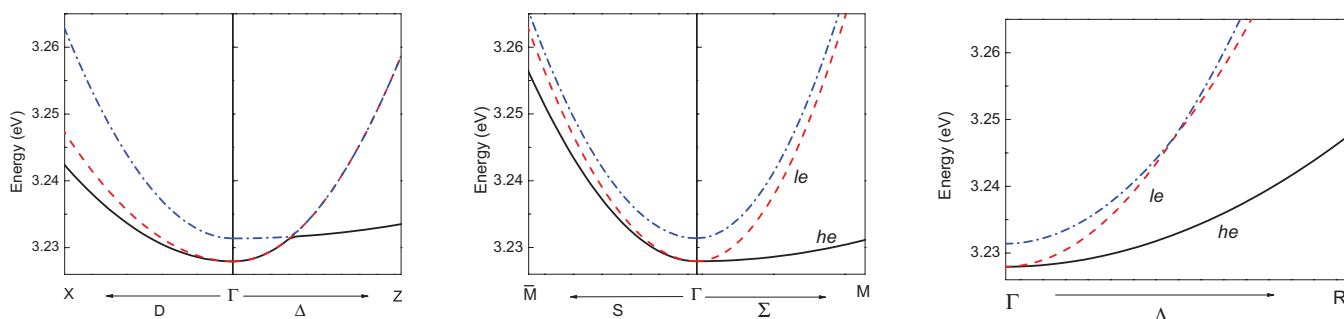


FIG. 1. (Color online) Enlargement of the region around calculated conduction band minimum (CBM) at the Γ point showing the splitting in SrTiO_3 caused by the AFD phase transition. The high-symmetry directions are those of the body-centered tetragonal lattice [100] (D), [001] (Δ) [101] (S), [110] (Σ), [111] (Λ), and $Z = (00\frac{1}{2})$ $\bar{M} = (\frac{1}{2}0\frac{1}{2})$.

TABLE II. Calculated lattice parameters of LAO as well as phase transition order parameters: the octahedral tilt angle (Θ) and the spontaneous strain ($\tau = c/a - \sqrt{6}$). Values with a reference number come from previous experimental and/or plane wave calculations.

	Rhombohedral					Cubic
	a (Å)	b (Å)	c (Å)	Θ (°)	τ	$a = b = c$ (Å)
Experiment ^a	5.365	5.365	13.111	5.7	-0.008	3.810 ^b
LSDA	5.341, 5.290 ^e	5.339	13.020	4.1, 6.1 ^e	-0.012	3.760, 3.750 ^c
PBE	5.448, 5.370 ^d	5.444, 5.370 ^d	13.250, 13.138 ^d	4.0	-0.017	3.830
HSE06	5.398	5.393	13.160	3.1	-0.011	3.800

^aAt 4.2 K from Ref. 66.

^bReference 69.

^cReference 70.

^dReference 71.

^eReference 72.

The combined HSE06 results, Δ_{CF}^{HSE06} and Δ_{SO}^{HSE06} , show an excellent *quantitative* agreement with experimental data obtained from single-domain Shubnikov–de Haas oscillation Raman spectroscopy measurements,⁶² namely, $\Delta_{CF}^{exp} = 2$ meV and $\Delta_{SO}^{exp} = 18$ meV. However, they do not support the picture proposed by the recent angle resolved photoemission spectroscopy (ARPES) experiment of Chang *et al.*,⁶¹ which indicates that the single band is of lower energy, with a doubly degenerate band 25 meV higher. This disagreement may arise from the fact that STO samples used in this experiment were doped with oxygen vacancies (V_O), which are known to introduce a shallow defect level in the band gap of STO.⁶⁴ Finally, using HSE06 and the TZVP basis set to model STO relaxed in the AFD phase, we found that the crystal field splits the CBM at the Γ point by 3 meV, leaving it doubly degenerate in the absence of SO coupling.

B. LaAlO₃

Bulk LaAlO₃ undergoes a phase transition from the simple cubic structure to a rhombohedral-central hexagonal structure with space group $R\bar{3}C$ at temperatures below 813 K.^{65–67} The two order parameters for this phase transition are the tilt of the AlO₆ octahedra (Θ), which can reach a maximum value of 5.7° at 4.2 K,⁶⁶ and τ , a measure of spontaneous strain, defined as $\tau = c/a - \sqrt{6}$, with values of up to -0.008. The calculated lattice parameters relative to experiment for both phases of bulk LAO are underestimated with LSDA, overestimated with PBE, and in between for HSE06 (Table II). This is well-known behavior for LSDA and PBE (see, e.g., Ref. 68 and references therein) and has been observed in a large number of semiconducting materials, as well as in our recent study on SrTiO₃.¹⁷

In the low-temperature rhombohedral phase, the LSDA and PBE lattice parameters tend to be higher than previous plane wave calculations.^{70–72} The octahedral tilt angle for both LSDA and PBE is about 4°, which is 30% smaller than the maximum tilts measured experimentally. The SZVP basis set produces tilt angles 30% lower than those observed by plane wave calculations⁷² which is very similar to the behavior we observed in the case of STO; we attribute this to the use of localized basis sets.¹⁷ HSE06 yields lattice parameters for the cubic phase in excellent agreement with experiment, with a deviation of only 0.25%, and improved rhombohedral lattice

parameters deviating by 0.5% compared to 1.5% with PBE. Improvement of the same magnitude was also obtained using the recently introduced variational pseudo self-interaction correction approach (VPSIC₀).⁷³

The calculated spontaneous strain (τ) is also significantly closer to experiment for HSE06 and LSDA than PBE. For all functionals considered here, the calculated lattice mismatch between cubic LAO and STO agree with the 2% value reported in the experiment, indicating that the basis set we used will not introduce any additional strain in LAO/STO superlattices beyond those inherently present in the experimentally measured ones.

Turning now to the electronic properties of LAO, our computed band gaps are summarized in Table III. Comparisons with experimental band gaps are relative to the room temperature rhombohedral phases since, to our knowledge, no experimental measurements of the cubic phase band gap exist.

In general, band gaps calculated using the LSDA and PBE are underestimated in average by ~30% or ~1.8 eV compared to experiment, with PBE doing better than the LSDA. This is consistent with earlier calculations^{70,71} and indicates that the basis set does not negatively impact electronic structure properties in a significant manner, a behavior we observed in the STO case as well.¹⁷ (Please see Table III for comparisons

TABLE III. Calculated band gaps of LaAlO₃ using the SZVP basis set compared to experimental values. Data from this work are listed first, followed by data from previous plane wave simulations and citations.

Band gap (eV)	Rhombohedral	Cubic	
	Direct	Indirect	Direct
Experiment	5.60 ^a		
LSDA	3.75, 3.87 ^e	3.25, 3.3 ^b	3.46
PBE	3.98, 3.95 ^c	3.27, 3.1 ^f	3.54
HSE06	5.24	4.77	5.04

^aReference 74.

^bReference 70.

^cReference 71.

^dReference 75.

^eReference 72.

^fReference 76.

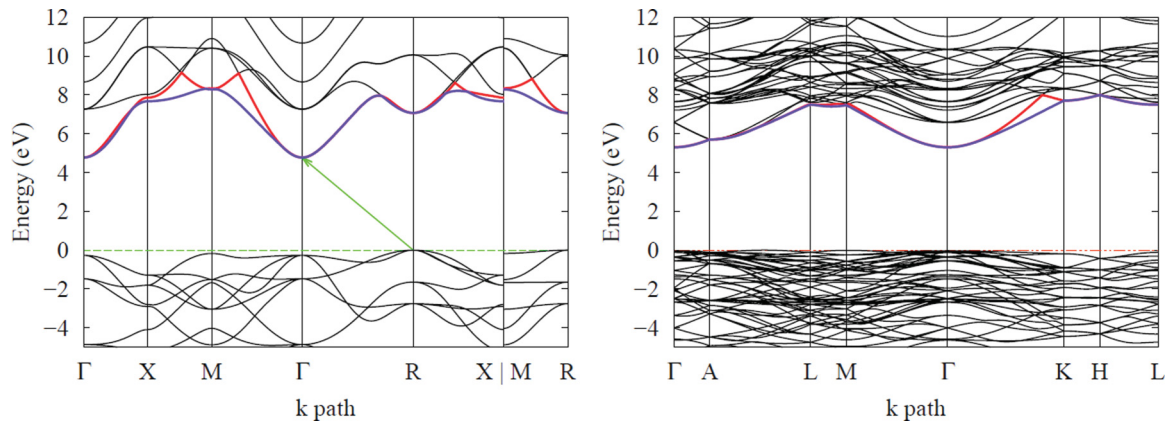


FIG. 2. (Color online) Band structure of LaAlO₃ calculated using HSE06 for the high-temperature cubic phase (left) and the low-temperature rhombohedral phase (right). The dashed line depicts the Fermi level at the valence band maximum (VBM).

with previous calculations.) As expected, HSE06 provides a much better estimate of the band gaps, even when using the smaller SZVP basis sets, with deviations from experiment not exceeding 0.36 eV or 6% for the rhombohedral phase. This error is larger than the 1% deviation observed in the SrTiO₃ case, but is well within the 0.3–0.4 eV range for nonionic bulk semiconductors.^{41–43,77}

For the cubic phase, HSE06 produces an indirect band gap of 4.7 eV, which agrees well with the calculated gap of 4.4 eV obtained using the screened exchange method^{76,78} (sX) and plane wave basis sets and the 4.61 eV gap obtained using the VPSIC₀ method.⁷³ The HSE06 direct gap is 5.0 eV, which lies between the VPSIC₀⁷³ value of 4.89 eV and the *GW*-corrected LSDA band gap at the experimental lattice constants⁷⁵ of 5.68 eV. The quality of the cubic phase results is encouraging for future heterostructure and defect state calculations because LAO films grown on Si substrates, using a few STO layers as a template, usually adopt the cubic structure.⁷⁹ The cubic and rhombohedral phase band structures as calculated by HSE06 for LaAlO₃ are shown in Fig. 2. They look very different because the Brillouin zone sampling and the number of atoms in each simulation supercell are different, but as we will demonstrate with the projected densities of states (PDOS), only small changes in the spectrum occur at the phase transition.

Starting from the cubic phase, the band gap is indirect ($R \rightarrow \Gamma$) with a doubly degenerate CBM and a triply degenerate valence band maximum (VBM). A close look at our computed CBM in the rhombohedral phase also reveals that the phase transition induces a lift of degeneracy at the CBM and a splitting at the Γ point with $\Delta_{CF} = 10$ meV. The band gap increase and Δ_{CF} for LAO are much higher than the values we reported for SrTiO₃; we attribute this to the fact that six of six oxygens are experiencing significant rigid octahedral tilts leading to changes in the La-O-La angles from the ideal 180° to 173.8°, compared to a smaller rotation resulting from a 4/6 oxygen ratio in the STO case.

By looking at the PDOS (Fig. 3) we observe that the VBM is strictly dominated by O-2*p* states, while La-5*d* states dominate the CBM. Unlike the SrTiO₃ case, no significant intermixing between the O-2*p* and La-5*d* states is observed, indicating that

the bonding has predominately ionic character. This picture is not affected by the phase transition, and no signs of orbital intermixing are observed in the rhombohedral phase PDOS as well, where peaks conserve their height and shape (not shown).

By aligning the VBM of both phases (see the bottom Fig. 3) we observe that the octahedral tilt leads to a shift of the CBM to higher energies, thus increasing the band gap by 500 meV. There is also experimental evidence that the crystal field caused by AlO₆ tilts in LaAlO₃ induces splitting of the CBM, but no quantitative values were reported.⁶⁶

In summary, by applying HSE06 to LAO we lose some agreement with experiment on the octahedral tilts but we gain better precision than semilocal functionals in the band gaps, lattice parameters, and strain altogether. In other words, overall HSE06 provides a more physically accurate picture.

C. LaTiO₃

LaTiO₃ adopts a *Pbnm*, GdFeO₃-type orthorhombic structure ($a \neq b \neq c$) with tilted and rotated TiO₆ octahedra (see Fig. 4) in the simulation supercell of 20 atoms, with no experimental evidence of a simpler cubic structure. The tolerance factor of a perovskite compound *ABO*₃, *t*, is defined as the ratio of the intrinsic sizes of the AO square and the BO₂ square.^{80,81}

$$t = \frac{r_A + r_O}{\sqrt{2}(r_B + r_O)}, \quad (1)$$

where r_A , r_B , and r_O are the ionic radii of each ion. In LaTiO₃, the tolerance factor is too small to favor the cubic structure due to the relative size of the La⁺³ ion to the TiO₆ octahedra.

Nevertheless, the octahedral tilts (Θ) stabilize the structure by shortening some La-O bonds [see Fig. 4(a)] and causing Ti-O₁-Ti angles to deviate from 180°. For any neighboring pair the TiO₆ octahedra would tilt around the *z* axis in opposite directions. The subsequent rotation with respect to the same axis (ϕ) is restricted to O₂ oxygens forming the basal plane of the TiO₆ and occur in the same sense. In addition, Cwik *et al.*⁶⁹ showed that the negative sign of their orthorhombic distortion parameter [$\epsilon = (b - a)/(b + a)$] demonstrates that the TiO₆ octahedra are distorted. The TiO₆ basal plane is rectangular-like

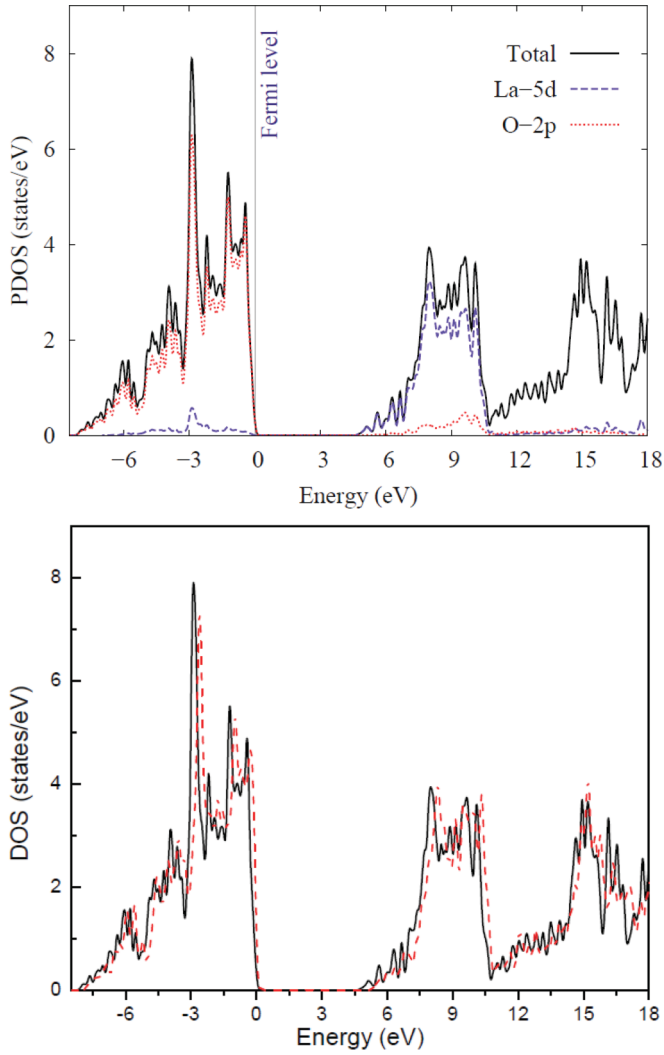


FIG. 3. (Color online) Top: Projected electronic densities of states (PDOS) for LaAlO_3 calculated using HSE06 in the cubic phase. Bottom: Changes in the total density of states upon the phase transition from cubic (solid line) to rhombohedral (dashed line) mainly characterized by a shift of the conduction band states to higher energies.

instead of cubic with the $\text{O}_2\text{-O}_2$ edge lengths splitting into $d_{\text{O}_2\text{-O}_2}^{\text{long}}$ and $d_{\text{O}_2\text{-O}_2}^{\text{short}}$ with a ratio

$$r_{\text{O}_2\text{-O}_2} = \frac{d_{\text{O}_2\text{-O}_2}^{\text{long}}}{d_{\text{O}_2\text{-O}_2}^{\text{short}}} \quad (2)$$

$r_{\text{O}_2\text{-O}_2}$ reaches up to 1.04 at 8 K. The octahedron's basal plane angles also deviate from the ideal 90° [see Fig. 4(c)] leading to differences in the Ti-O_2 distances, namely, $d_{\text{Ti-O}_2}^{\text{long}}$ and $d_{\text{Ti-O}_2}^{\text{short}}$ and the ratio

$$r_{\text{Ti-O}_2} = \frac{d_{\text{Ti-O}_2}^{\text{long}}}{d_{\text{Ti-O}_2}^{\text{short}}} \quad (3)$$

LaTiO_3 undergoes a phase transition from a nonmagnetic insulator to an antiferromagnetic Mott insulator at temperatures near $T_c = 146$ K without undergoing important changes in the structural parameters.⁶⁹ To determine the initial

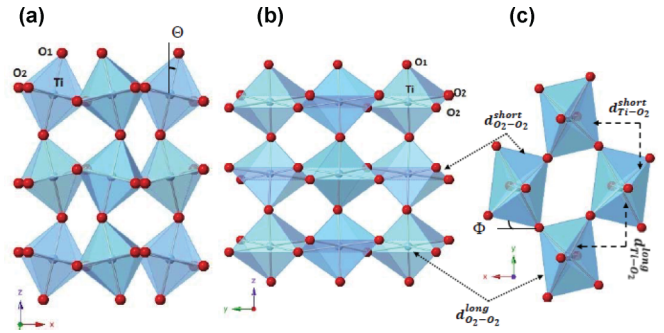


FIG. 4. (Color online) Tilted and rotated TiO_6 octahedra in LaTiO_3 viewed along (a) 010 direction showing the octahedral tilts (Θ) with respect to the z axis, (b) 100 direction featuring the rectangular-like basal plane of the TiO_6 octahedra, and (c) 001 direction showing clearly the octahedral rotation (Φ), the orthorhombic distortion, and the different interatomic distances arising from it. Note that the lattice parameters b have been increased by 35% for a better illustration of basal plane distortion.

geometry for LTO, we fully relaxed a nonmagnetic 20-atom LTO supercell with the PBE and HSE06 functionals, starting from several experimental structures acquired at different temperatures.^{69,82,83} All structures relaxed to the same minimum. The lattice parameters of the fully relaxed nonmagnetic structure with both PBE and HSE06 are summarized in Table IV and compared to experimental data taken at $T = 155$ K just above the phase transition temperature.

Using HSE06, we observe excellent agreement with experiment as shown by the orthorhombic distortion parameter⁸⁴ (ϵ) being of the right sign and magnitude. In addition, $r_{\text{O}_2\text{-O}_2}$ and $r_{\text{Ti-O}_2}$ ratios compare very well with experiment,^{69,82} an indication that the octahedral distortion is well reproduced. With PBE, ϵ has a positive sign which suggests that the TiO_6 octahedra elongate along b instead of a which qualitatively incorrect. The last behavior has been reported previously in Ref. 28 as a drawback of LSDA that have been overcome by adding the adequate U correction⁸⁵ (see the LSDA + U results in Table IV). Also, $r_{\text{O}_2\text{-O}_2}$ and $r_{\text{Ti-O}_2}$ ratios indicate that TiO_6 octahedra are nearly ideal and do not reproduce the distortion observed experimentally. The octahedral tilt (Θ) and rotation angles (Φ) are underestimated by 2° and 0.45° , respectively, with HSE06, but the underestimation is worse in the PBE case, reaching 3.3° and 2.85° , respectively.

Turning to the electronic properties, the calculated projected density of states for LaTiO_3 in the nonmagnetic state (Fig. 5) are similar for HSE06 and PBE showing metallic behavior and a Fermi level lying at the middle of the Ti-3d band.⁸⁶ The Ti-3d band is separated from the O-2p band by 3.95 and 2.87 eV for HSE06 and PBE, respectively. As with SrTiO_3 , the valence band (VB) is dominated by O-2p states while the conduction band is dominated by Ti-3d states with some intermixing between O-2p and Ti-3d orbitals, indicating a partially covalent bond.

The band structure in the bottom of Fig. 5 shows more details about the O-2p and Ti-3d band separation where the t_{2g} triplet states^{87,88} can be distinguished by their colors. The GdFeO_3 -type distortion causes a large crystal-field splitting (Δ_{CF}) defined as the separation between the two first t_{2g} triplet

TABLE IV. Lattice constants and orthorhombic distortion parameters as well as octahedral tilt (Θ) and rotation angles (Φ) calculated using SZVP basis set for the fully relaxed LaTiO₃ structures. Comparison is done with experimental data taken at 155 K from Ref. 69 near the magnetic to antiferromagnetic transition temperature $T_N = 146$ K.

	a (Å)	b (Å)	c (Å)	ϵ	$r_{\text{O}_2-\text{O}_2}^{\text{d}}$	$r_{\text{Ti}-\text{O}_2}^{\text{d}}$	Θ (°)	Φ (°)
Experiment ^a	5.635	5.602	7.905	-0.0030	1.035	1.011	12.86	9.69
HSE06	5.600	5.534	7.904	-0.0059	1.027	1.013	10.88	9.25
PBE	5.595	5.632	7.938	+0.0033	1.008	0.998	9.54	6.85
LSDA ^b	5.462	5.524	7.789	+0.0056				
LSDA + U^{c}	5.586	5.529	7.89	-0.0051				

^aAt 155 K from Ref. 69.

^bReference 28.

^cFor the optimum values of $U = 3.2$ and $J = 0.9$ eV identified in Ref. 28.

^dDistances evaluated for the same set of reference atoms.

states^{87,88} at the Γ point and a subsequent smaller splitting (Δ'_{CF}) between the second and the third states. The amount of Δ_{CF} is strongly correlated to the orbital state of LTO (see the review paper of Mochizuki and Imada⁸⁹ and the recent paper of Krivenko⁸⁸) with small CFS inducing an orbital liquid state^{85,90} while large CFS favors an induced orbital ordering.^{73,91-93}

With HSE06, Δ_{CF} is about 410 meV, somewhat larger than the experimental splittings of 240 meV⁶⁹ and 300 meV⁹¹ evaluated for nonmagnetic solutions. With PBE, we find a much smaller Δ_{CF} of 61 meV, which is consistent with LSDA + U calculations ranging between 37 and 54 meV.^{90,94} This small CFS is a shared feature between semilocal functionals and might be at the origin of the unsettled theoretical description of the orbital state of bulk LaTiO₃.^{88,89} With HSE06, $\Delta'_{\text{CF}} = 190$ meV which is high compared to the nearly degenerate

doublet observed experimentally.⁶⁹ This difference probably comes from the higher orthorhombic distortion we observe in our defect-free relaxed structures which is known experimentally to increase with decreasing defect concentration.⁶⁹

Turning now to the properties of magnetic solutions, the experiments of Cwik *et al.*⁶⁹ reveal almost no difference in the structural properties between the magnetic and nonmagnetic solutions close to the transition temperature. Based on that, we assume that the calculated structure in the magnetic state does not differ much from the nonmagnetic one near the transition temperature leading to $\Delta_{\text{CF}}^{\text{nonmagn}} = \Delta_{\text{CF}}^{\text{magn}}$. Thus, the total splitting of the t_{2g} states in a magnetic state ($\Delta_{\text{tot}}^{\text{magn}}$) is a result of the interplay between $\Delta_{\text{CF}}^{\text{nonmagn}}$ due to the structural GdFeO₃ distortion and spin superexchange splitting (Δ_{SE}).

TABLE V. Calculated HSE06 energy differences referenced to the G-type antiferromagnetic (AFM) ground state (ΔE), the Mott gap (M_{gap}), the charge transfer gap (Δ), and the magnetic moments (μ) for the Ti atoms as obtained from the Mulliken population analysis of the spin density. The separation between the O-2*p* states and the first Ti-3*d* states (Δ_{pd}), the width of the Mott band (E_M), and the value of the first splitting of the t_{2g} at the Γ point ($\Delta_{\text{tot}}^{\text{magn}}$) are also reported.

	Spin	ΔE (meV)	M_{gap} (eV)	Δ (eV)	μ (a.u.)	Δ_{pd} (eV)	E_M (eV)	$\Delta_{\text{tot}}^{\text{magn}}$ (meV)
AFM: G Type								
Experiment			0.1-0.2	4.5	0.57 ^a , 0.45 ^b	3.0 ^b		120-300 ^c
Prev. Calcs.			1.6 ^c , 0.57 ^d 0.77 ^e	5.2 ^c , 3.5 ^d	0.89 ^c , 0.78 ^d 0.68 ^e	3.1 ^c , 2.3 ^d		400 ^c , 230 ^d 140 ^f , 54 ^g
This Work								
AFM G-Type	$\uparrow \downarrow$ $\downarrow \uparrow$	0	1.27	5.2	0.94	2.9	1.0	700
AFM A-Type	$\uparrow \downarrow$ $\downarrow \uparrow$	21	1.39	5.0	0.90	3.0	0.6	326
AFM C-Type	$\uparrow \downarrow$ $\downarrow \uparrow$	44	0.93	4.9	0.92	2.9	1.4	660
FM	$\uparrow \downarrow$ $\downarrow \uparrow$	795	1.02	5.2	0.92	2.5	1.8	720

^aReference 69.

^bReference 95.

^cReference 91.

^dVPSIC results from Ref. 73 for relaxed internal coordinates using the lattice parameters fixed to experimental values.

^eLDA + U results from Ref. 92 using the experimental LaTiO₃ structure at 8 K from Ref. 69.

^fDFT + U + GWA from Ref. 96.

^gLDA + U results from Ref. 97.

^hLDA + U results from Ref. 90.

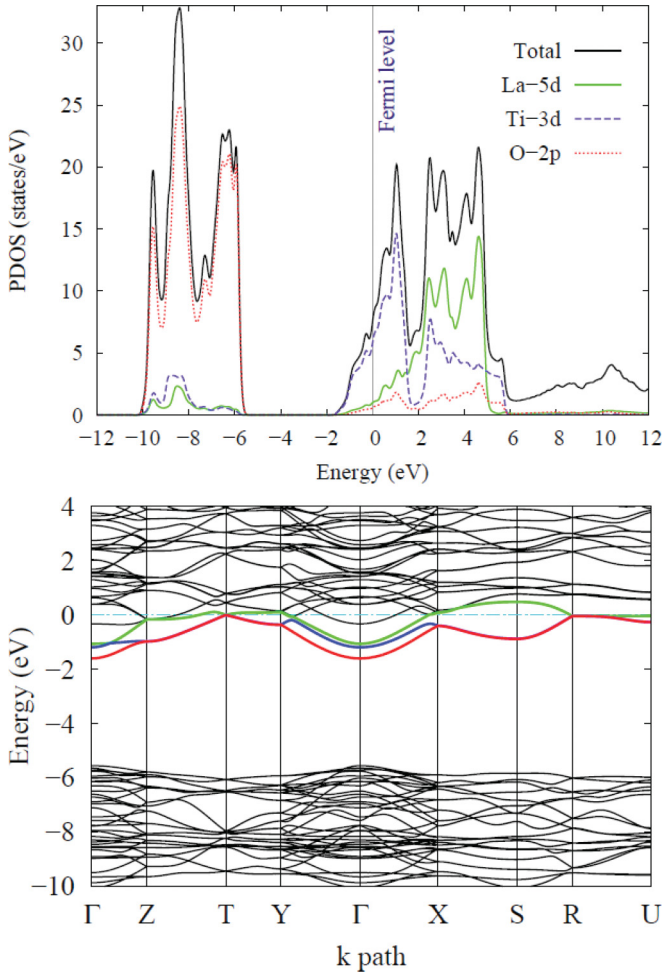
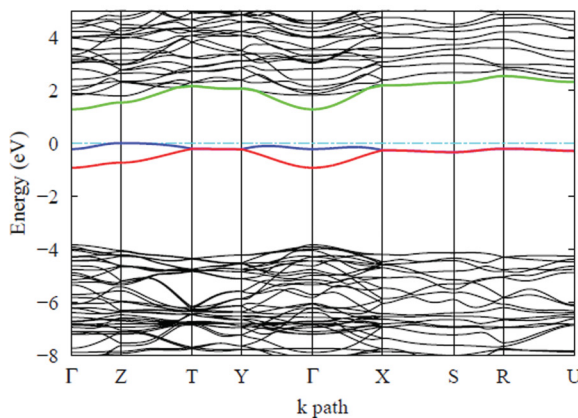


FIG. 5. (Color online) Top: Total and projected density of states for orthorhombic LaTiO_3 as calculated with HSE06 and the SZVP basis set. Only the contribution from the dominant states is represented. Bottom: The corresponding band structure of LaTiO_3 in the nonmagnetic state. The Ti t_{2g} triplet bands can be distinguished by their colors where the splittings caused by octahedral deformation can be clearly seen.



The nonmagnetic minimum was used for subsequent *unrestricted* spin calculations where spin flips were carried out to simulate, using the same parameters, the ferromagnetic (FM) and G-type, A-type, and C-type antiferromagnetic (AFM) states (see Table V and Ref. 98 for a description of the different magnetic orderings). We have two reasons for considering the different magnetic states: First, we want to test the ability of HSE06 to identify the ground state because previous calculation with LDA + U ⁹² predicted the A-type AFM state to be the ground state, which is in disagreement with the G-type AFM state found experimentally. Second, those different magnetic orders might not be observed in bulk LTO under normal conditions, but might become relevant under strain or for LTO-based heterostructures. Thus, details of electronic structure of LTO in all magnetic states will be examined with focus on $\Delta_{\text{tot}}^{\text{magn}}$.

In the ferromagnetic and antiferromagnetic spin orientations, PBE predicts LTO as metallic, whereas experiment has shown it to be a Mott insulator.⁶⁹ This is a well-known limitation of semilocal functionals and agrees very well with the conclusions from early DFT studies of LTO using plane wave basis sets.^{28,86,99,100} This has been overcome in the past by adding the Coulomb term correction (U) or via a GW correction.^{96,101} HSE06 performs much better than PBE predicting the G-type AFM ordering to be the ground state and a Mott insulator.⁶⁹ LaTiO_3 also transforms to a Mott insulator for the other magnetic orders we considered, with an energy gain relative to ground state of 21 meV for A-type AFM, 44 meV for C-type AFM, and 795 meV for the FM states.

The band structure of a Mott insulator is characterized by the optical gap, which is determined by the Hubbard splitting (M_{gap}) of the d -band separation of the lower and upper Hubbard bands; this is also called the Mott gap. The other gap is called the charge transfer gap, which is the energy difference (Δ) between the filled p bands and the unoccupied upper Hubbard $3d$ band. For LaTiO_3 , the experimental Mott gap is 0.1 eV according to the measurements of Arima *et al.*¹⁰² while the CT gap is 4.5 eV.

The nature of the band gap (direct vs indirect), the shape and the width of the Mott bands, as well as the amount of $\Delta_{\text{tot}}^{\text{magn}}$ are discussed below: In the G-type AFM (Fig. 6), the gap is indirect from $Z \rightarrow \Gamma$ and measures 1.27 eV, separating

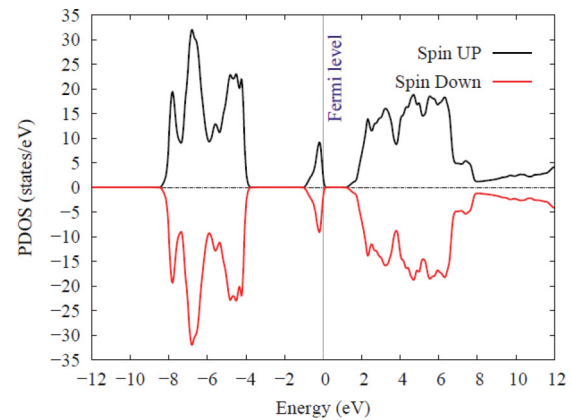


FIG. 6. (Color online) Band structure and PDOS for LaTiO_3 in the G-type antiferromagnetic spin orientation. The Ti t_{2g} triplet bands can be distinguished by their colors and $\Delta_{\text{tot}}^{\text{magn}}$ is evaluated from the separation of the two bottom ones.

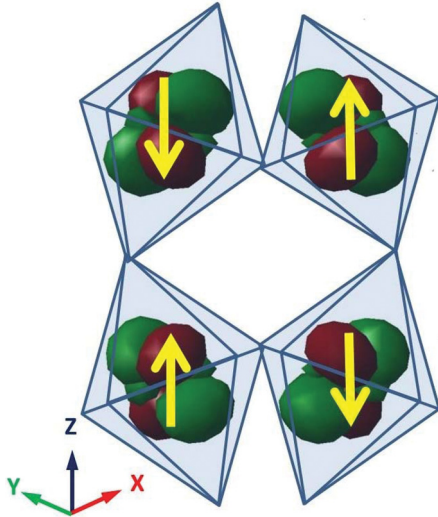


FIG. 7. (Color online) Isosurface of the highest occupied t_{2g} state orbitals for G-type AFM LaTiO_3 at the Γ special k point. Orbitals show an antiferro-orbital ordering alternating between d_{xz} and d_{yz} orientations between each neighboring TiO_6 octahedra. Arrows indicate the antiferromagnetic spin orientation on Ti sublattice.

the occupied lower Hubbard band from the unoccupied higher Hubbard band; the Mott band is 1 eV, showing a $\Delta_{\text{tot}}^{\text{magn}}$ of 700 meV. In the A-type AFM ordering we observe a larger, indirect band gap from $R \rightarrow \Gamma$ of 1.39 eV, but a narrower Mott band (sharper and thinner) due to the reduced splitting between the t_{2g} states, about 320 meV. In the C-type AFM spin orientation, the indirect gap from $S \rightarrow \Gamma$ has the smallest value, 0.9 eV, but $\Delta_{\text{tot}}^{\text{magn}}$ is comparable to the G-type ordering value while the Mott band is larger by 0.4 eV. In the FM state, we find a direct band gap of 1 eV and $\Delta_{\text{tot}}^{\text{magn}}$ comparable to the G-type ordering value while the Mott band is larger by 0.8 eV.

Our calculated Mott gaps, CT gaps, and magnetic moments for various magnetic orders are summarized in Table V and compared to experiments and previous calculations. The separation between the O-2p states and the first Ti-3d states (Δ_{pd}), the width of the Mott band (E_M), as well as the value of the first splitting of the t_{2g} at the Γ point ($\Delta_{\text{tot}}^{\text{magn}}$) are also reported. In the G-type AFM ground state, our HSE06 value for $\Delta_{pd} = 2.9$ eV is in excellent agreement with the 3 eV value reported experimentally.⁹⁵ Also, the CT gap is only 0.5 eV higher than the experimentally measured value of 4.5 eV, which constitutes an improvement over the previous LDA + U calculation.⁹² However, M_{gap} and μ are higher than the experimentally reported values. This overestimation obtained with HSE06 was addressed in the recent study of Rivero *et al.*,²³ which demonstrated that screened hybrids do provide a good *quantitative* description of the electronic structure of strongly correlated systems, but that

the magnetic coupling constants remain overestimated^{103–105} compared to experiment. This phenomenon is observed using other theoretical methods^{73,86,90,92,96,97} summarized in Table V, and several explanations for this widespread divergence of theory and experiment have been proposed.^{73,89} It is very likely that the experimental samples are not pristine and contain defects which “metallize” them, yielding smaller gaps.

Based on our HSE06 large Δ_{CF} and μ values, LTO is expected to display an induced orbital order. Indeed, orbital ordering in G-type AFM LaTiO_3 can be clearly seen in Fig. 7 showing the highest occupied t_{2g} state orbitals for G-type AFM LaTiO_3 at the Γ special k point. Orbitals show an antiferro-orbital ordering oriented parallel to the z axis and oriented along the long Ti-O₂ bonds. Because the *long* Ti-O₂ bonds [see Fig. 4(c)] are perpendicular between each neighboring TiO_6 octahedra, the orbitals sitting along those bonds appear alternating between d_{xz} and d_{yz} and tilted due to the GdFeO_3 distortion. This picture confirms once again experiments⁹¹ and theoretical calculations⁸⁹ suggesting that LaTiO_3 has an induced orbital order and might not be an orbital liquid.

IV. CONCLUSIONS

The performance of the screened hybrid HSE06 was tested for modeling the fully relaxed semiconducting metal oxide perovskites SrTiO_3 and LaAlO_3 in their different structural phases, and the strongly correlated Mott insulator LaTiO_3 in the ferromagnetic and various antiferromagnetic orderings. HSE06 gives good band gaps and accurate structural/geometric properties. It demonstrated great efficiency in handling structural phase transitions, and yielded accurate structural properties and order parameters (octahedral rotations/tilts and strains) for all three perovskites. This is a substantial improvement over DFT + U , one that suggests that HSE06 may be as successful in treating other metal oxides and the metal-insulator transition in oxide superlattices. In addition, the crystal-field splitting (Δ_{CF}) of the t_{2g} states resulting from the phase transitions in SrTiO_3 , LaAlO_3 , and LaTiO_3 was evaluated for all three materials, and showed excellent agreement with experiment in the STO case.⁶² The LTO computed $\Delta_{\text{CF}} = 410$ meV is rather high and indicates that LaTiO_3 has an induced orbital order that is clearly shown from our analysis of highest occupied t_{2g} state orbitals.

ACKNOWLEDGMENTS

This work is supported by the Qatar National Research Fund (QNRF) through the National Priorities Research Program (NPRP 08-431-1-076). We are grateful to the research computing facilities at Texas A&M University at Qatar for generous allocations of computer resources.

*fadwa.el_mellouhi@qatar.tamu.edu

†ed.brothers@qatar.tamu.edu

¹J. Chakhalian, A. J. Millis, and J. Rondinelli, *Nat. Mater.* **11**, 92 (2012).

²H. Y. Hwang, Y. Iwasa, M. Kawasaki, B. Keimer, N. Nagaosa, and Y. Tokura, *Nat. Mater.* **11**, 103 (2012).

³R. Pentcheva and W. E. Pickett, *J. Phys.: Condens. Matter* **22**, 043001 (2010).

- ⁴P. Zubko, S. Gariglio, M. Gabay, P. Ghosez, and J.-M. Triscone, *Annu. Rev. Condens. Matter Phys.* **2**, 141 (2011).
- ⁵G. Kotliar, S. Y. Savrasov, K. Haule, V. S. Oudovenko, O. Parcollet, and C. A. Marianetti, *Rev. Mod. Phys.* **78**, 865 (2006).
- ⁶K. Held, I. A. Nekrasov, G. Keller, V. Eyert, N. Blümer, A. K. McMahan, R. T. Scalettar, T. Pruschke, V. I. Anisimov, and D. Vollhardt, *Phys. Status Solidi B* **243**, 2599 (2006).
- ⁷D. Vollhardt, *Ann. Phys.* **524**, 1 (2012).
- ⁸G. Onida, L. Reining, and A. Rubio, *Rev. Mod. Phys.* **74**, 601 (2002).
- ⁹G. Trimarchi, H. Peng, J. Im, A. J. Freeman, V. Cloet, A. Raw, K. R. Poepelmeier, K. Biswas, S. Lany, and A. Zunger, *Phys. Rev. B* **84**, 165116 (2011).
- ¹⁰A. Franceschetti and A. Zunger, *Nature (London)* **402**, 60 (1999).
- ¹¹J. M. Rondinelli and N. A. Spaldin, *Phys. Rev. B* **82**, 113402 (2010).
- ¹²N. A. Benedek, A. T. Mulder, and C. J. Fennie, *J. Solid State Chem.* **195**, 11 (2012).
- ¹³S. S. A. Seo, M. J. Han, G. W. J. Hassink, W. S. Choi, S. J. Moon, J. S. Kim, T. Susaki, Y. S. Lee, J. Yu, C. Bernhard, H. Y. Hwang, G. Rijnders, D. H. A. Blank, B. Keimer, and T. W. Noh, *Phys. Rev. Lett.* **104**, 036401 (2010).
- ¹⁴P. Aguado-Puente, P. García-Fernández, and J. Junquera, *Phys. Rev. Lett.* **107**, 217601 (2011).
- ¹⁵B. Jalan, S. J. Allen, G. E. Beltz, P. Moetakef, and S. Stemmer, *Appl. Phys. Lett.* **98**, 132102 (2011).
- ¹⁶A. Janotti, D. Steiauf, and C. G. Van de Walle, *Phys. Rev. B* **84**, 201304 (2011).
- ¹⁷F. El-Mellouhi, E. N. Brothers, M. J. Lucero, and G. E. Scuseria, *Phys. Rev. B* **84**, 115122 (2011).
- ¹⁸J. P. Perdew and Y. Wang, *Phys. Rev. B* **45**, 13244 (1992).
- ¹⁹J. P. Perdew, K. Burke, and M. Ernzerhof, *Phys. Rev. Lett.* **77**, 3865 (1996).
- ²⁰J. P. Perdew, K. Burke, and M. Ernzerhof, *Phys. Rev. Lett.* **78**, 1396 (1997).
- ²¹V. N. Staroverov, G. E. Scuseria, J. Tao, and J. P. Perdew, *J. Chem. Phys.* **119**, 12129 (2003).
- ²²V. N. Staroverov, G. E. Scuseria, J. Tao, and J. P. Perdew, *J. Chem. Phys.* **121**, 11507 (2004).
- ²³P. Rivero, I. P. R. Moreira, G. E. Scuseria, and F. Illas, *Phys. Rev. B* **79**, 245129 (2009).
- ²⁴Y. F. Zhukovskii, E. A. Kotomin, S. Piskunov, and D. E. Ellis, *Solid State Commun.* **149**, 1359 (2009).
- ²⁵E. Heifets, E. Kotomin, and V. A. Trepakov, *J. Phys.: Condens. Matter* **18**, 4845 (2006).
- ²⁶S. Piskunov, E. Heifets, R. I. Eglitis, and G. Borstel, *Comput. Mater. Sci.* **29**, 165 (2004).
- ²⁷D. I. Bilc, R. Orlando, R. Shaltaf, G. M. Rignanese, J. Íñiguez, and P. Ghosez, *Phys. Rev. B* **77**, 165107 (2008).
- ²⁸H.-S. Ahn, D. D. Cuong, J. Lee, and S. Han, *J. Korean Phys. Soc.* **49**, 1536 (2006).
- ²⁹U. Schwingenschlögl and C. Schuster, *Chem. Phys. Lett.* **467**, 354 (2009).
- ³⁰S. Gemming and G. Seifert, *Acta Mater.* **54**, 4299 (2006).
- ³¹V. Pardo and W. E. Pickett, *Phys. Rev. B* **81**, 245117 (2010).
- ³²J. Lee and A. A. Demkov, *Phys. Rev. B* **78**, 193104 (2008).
- ³³P. V. Ong, J. Lee, and W. E. Pickett, *Phys. Rev. B* **83**, 193106 (2011).
- ³⁴A. D. Becke, *J. Chem. Phys.* **98**, 5648 (1993).
- ³⁵P. J. Stephens, F. J. Devlin, C. F. Chabalowski, and M. J. Frisch, *J. Phys. Chem.* **98**, 11623 (1994).
- ³⁶C. Lee, W. Yang, and R. G. Parr, *Phys. Rev. B* **37**, 785 (1988).
- ³⁷D. I. Bilc, R. Orlando, R. Shaltaf, G. M. Rignanese, J. Íñiguez, and P. Ghosez, *Phys. Rev. B* **77**, 165107 (2008).
- ³⁸R. I. Eglitis and D. Vanderbilt, *Phys. Rev. B* **77**, 195408 (2008).
- ³⁹J. Heyd, G. E. Scuseria, and M. Ernzerhof, *J. Chem. Phys.* **124**, 219906 (2006).
- ⁴⁰T. M. Henderson, A. F. Izmaylov, G. E. Scuseria, and A. Savin, *J. Theor. Comput. Chem.* **4**, 1254 (2008).
- ⁴¹M. J. Lucero, T. M. Henderson, and G. E. Scuseria, *J. Phys.: Condens. Matter* **24**, 145504 (2012).
- ⁴²T. M. Henderson, J. Paier, and G. E. Scuseria, *Phys. Status Solidi B* **248**, 767 (2011).
- ⁴³B. G. Janesko, T. M. Henderson, and G. E. Scuseria, *Phys. Chem. Chem. Phys.* **11**, 443 (2009).
- ⁴⁴T. M. Henderson, B. G. Janesko, and G. E. Scuseria, *J. Phys. Chem. A* **112**, 12530 (2008).
- ⁴⁵R. Wahl, D. Vogtenhuber, and G. Kresse, *Phys. Rev. B* **78**, 104116 (2008).
- ⁴⁶Y. Yamada and Y. Kanemitsu, *Phys. Rev. B* **82**, 121103 (2010).
- ⁴⁷J. Paier, M. Marsman, G. Kresse, I. C. Gerber, and J. G. Ángyán, *J. Chem. Phys.* **124**, 154709 (2006).
- ⁴⁸M. Marsman, J. Paier, A. Stroppa, and G. Kresse, *J. Phys.: Condens. Matter* **20**, 064201 (2008).
- ⁴⁹J. Heyd, G. E. Scuseria, and M. Ernzerhof, *J. Chem. Phys.* **118**, 8207 (2003).
- ⁵⁰O. A. Vydrov and G. E. Scuseria, *J. Chem. Phys.* **125**, 234109 (2006).
- ⁵¹J. J. Phillips and J. E. Peralta, *J. Chem. Phys.* **134**, 034108 (2011).
- ⁵²M. J. Frisch *et al.*, GAUSSIAN development version, revision h.07+ (Gaussian, Inc., Wallingford, CT).
- ⁵³K. N. Kudin and G. E. Scuseria, *Phys. Rev. B* **61**, 16440 (2000).
- ⁵⁴ICSD, Inorganic Crystallographic Structural Database, http://www.fiz-karlsruhe.de/icsd_web.html (2010); specifically, the ICSD collection ID numbers are STO cubic 94573, AFD 56718; LAO rhomb 92554, cubic 92561; LTO 8146, 98414, 98416, and 63573.
- ⁵⁵F. Weigend and R. Ahlrichs, *Phys. Chem. Chem. Phys.* **7**, 3297 (2005).
- ⁵⁶S. H. Vosko, L. Wilk, and M. Nusair, *Can. J. Phys.* **58**, 1200 (1980).
- ⁵⁷CCDC 900592-900596 contains the supplementary crystallographic data for this paper. These data can be obtained free of charge from the Cambridge Crystallographic Data Centre via http://www.ccdc.cam.ac.uk/data_request/cif.
- ⁵⁸H. Unoki and T. Sakudo, *J. Phys. Soc. Jpn.* **23**, 546 (1967).
- ⁵⁹A. Heidemann and H. Wettengel, *Z. Phys.* **258**, 429 (1973).
- ⁶⁰R. Bistritzer, G. Khalsa, and A. H. MacDonald, *Phys. Rev. B* **83**, 115114 (2011).
- ⁶¹Y. J. Chang, A. Bostwick, Y. S. Kim, K. Horn, and E. Rotenberg, *Phys. Rev. B* **81**, 235109 (2010).
- ⁶²H. Uwe, R. Yoshizaki, T. Sakudo, A. Izumi, and T. Uzumaki, *Jpn. J. Appl. Phys., Part 1* **24**, 335 (1985).
- ⁶³L. F. Mattheiss, *Phys. Rev. B* **6**, 4740 (1972).
- ⁶⁴Z. Q. Liu, D. P. Leusink, X. Wang, W. M. Lü, K. Gopinadhan, A. Annadi, Y. L. Zhao, X. H. Huang, S. W. Zeng, Z. Huang, A. Srivastava, S. Dhar, T. Venkatesan, and Ariando, *Phys. Rev. Lett.* **107**, 146802 (2011).
- ⁶⁵C. J. Howard, B. J. Kennedy, and B. C. Chakoumakos, *J. Phys.: Condens. Matter* **12**, 349 (2000).

- ⁶⁶S. A. Hayward, F. D. Morrison, S. A. T. Redfern, E. K. H. Salje, J. F. Scott, K. S. Knight, S. Tarantino, A. M. Glazer, V. Shuvaeva, P. Daniel, M. Zhang, and M. A. Carpenter, *Phys. Rev. B* **72**, 054110 (2005).
- ⁶⁷H. Lehnert, H. Boysen, J. Schneider, F. Frey, D. Hohlwein, P. Radaelli, and H. Ehrenberg, *Z. Kristallogr.* **215**, 536 (2000).
- ⁶⁸P. Mori-Sánchez, A. J. Cohen, and W. Yang, *Phys. Rev. Lett.* **100**, 146401 (2008).
- ⁶⁹M. Cwik, T. Lorenz, J. Baier, R. Müller, G. André, F. Bourée, F. Lichtenberg, A. Freimuth, R. Schmitz, E. Müller-Hartmann, and M. Braden, *Phys. Rev. B* **68**, 060401 (2003).
- ⁷⁰A. A. Knizhnik, I. M. Iskandarova, A. A. Bagaturyants, B. V. Potapkin, L. R. C. Fonseca, and A. Korkin, *Phys. Rev. B* **72**, 235329 (2005).
- ⁷¹X. Luo and B. Wang, *J. Appl. Phys.* **104**, 053503 (2008).
- ⁷²H. Seo and A. A. Demkov, *Phys. Rev. B* **84**, 045440 (2011).
- ⁷³A. Filippetti, C. D. Pemmaraju, S. Sanvito, P. Delugas, D. Puggioni, and V. Fiorentini, *Phys. Rev. B* **84**, 195127 (2011).
- ⁷⁴S.-G. Lim, S. Kriventsov, T. N. Jackson, J. H. Haeni, D. G. Schlom, A. M. Balbashov, R. Uecker, P. Reiche, J. L. Freeouf, and G. Lucovsky, *J. Appl. Phys.* **91**, 4500 (2002).
- ⁷⁵X. Luo, B. Wang, and Y. Zheng, *Phys. Rev. B* **80**, 104115 (2009).
- ⁷⁶K. Xiong, J. Robertson, and S. J. Clark, *Microelectron. Eng.* **85**, 65 (2008).
- ⁷⁷Y.-i. Matsushita, K. Nakamura, and A. Oshiyama, *Phys. Rev. B* **84**, 075205 (2011).
- ⁷⁸J. Robertson, K. Xiong, and S. J. Clark, *Phys. Status Solidi B* **243**, 2054 (2006).
- ⁷⁹J. W. Reiner, A. Posadas, M. Wang, M. Sidorov, Z. Krivokapic, F. J. Walker, T. P. Ma, and C. H. Ahn, *J. Appl. Phys.* **105**, 124501 (2009).
- ⁸⁰V. M. Goldsmith, *Geochemische Verteilungsgesetze der Elemente VII-VIII* (1928).
- ⁸¹K. Uchida, S. Tsuneyuki, and T. Schimizu, *Phys. Rev. B* **68**, 174107 (2003).
- ⁸²M. Eitel and J. E. Greedan, *J. Less-Common Met.* **116**, 95 (1986).
- ⁸³D. A. MacLean, H.-N. Ng, and J. E. Greedan, *J. Solid State Chem.* **30**, 35 (1979).
- ⁸⁴C. J. Pickard, B. Winkler, R. K. Chen, M. C. Payne, M. H. Lee, J. S. Lin, J. A. White, V. Milman, and D. Vanderbilt, *Phys. Rev. Lett.* **85**, 5122 (2000).
- ⁸⁵I. Solovyev, N. Hamada, and K. Terakura, *Phys. Rev. B* **53**, 7158 (1996).
- ⁸⁶S. Okatov, A. Poteryaev, and A. Lichtenstein, *Europhys. Lett.* **70**, 499 (2005).
- ⁸⁷E. Pavarini, A. Yamasaki, J. Nuss, and O. K. Andersen, *New J. Phys.* **7**, 188 (2005).
- ⁸⁸S. Krivenko, *Phys. Rev. B* **85**, 064406 (2012).
- ⁸⁹M. Mochizuki and M. Imada, *New J. Phys.* **6**, 154 (2004).
- ⁹⁰I. V. Solovyev, *Phys. Rev. B* **69**, 134403 (2004).
- ⁹¹M. W. Haverkort *et al.*, *Phys. Rev. Lett.* **94**, 056401 (2005).
- ⁹²S. V. Streltsov, A. S. Mylnikova, A. O. Shorikov, Z. V. Pchelkina, D. I. Khomskii, and V. I. Anisimov, *Phys. Rev. B* **71**, 245114 (2005).
- ⁹³J.-G. Cheng, Y. Sui, J.-S. Zhou, J. B. Goodenough, and W. H. Su, *Phys. Rev. Lett.* **101**, 087205 (2008).
- ⁹⁴I. V. Solovyev, *Phys. Rev. B* **74**, 054412 (2006).
- ⁹⁵J. P. Goral and J. E. Greedan, *J. Magn. Magn. Mater.* **37**, 315 (1983).
- ⁹⁶Y. Nohara, S. Yamamoto, and T. Fujiwara, *Phys. Rev. B* **79**, 195110 (2009).
- ⁹⁷E. Pavarini, S. Biermann, A. Poteryaev, A. I. Lichtenstein, A. Georges, and O. K. Andersen, *Phys. Rev. Lett.* **92**, 176403 (2004).
- ⁹⁸J. B. Goodenough, *Phys. Rev.* **100**, 564 (1955).
- ⁹⁹N. Hamada, H. Sawada, I. Solovyev, and K. Terakura, *Physica B: Condensed Matter* **237–238**, 11 (1997).
- ¹⁰⁰G. Pari, S. Mathi Jaya, G. Subramoniam, and R. Asokamani, *Phys. Rev. B* **51**, 16575 (1995).
- ¹⁰¹I. V. Solovyev, *J. Phys.: Condens. Matter* **20**, 293201 (2008).
- ¹⁰²T. Arima, Y. Tokura, and J. B. Torrance, *Phys. Rev. B* **48**, 17006 (1993).
- ¹⁰³I. D. Prodan, G. E. Scuseria, and R. L. Martin, *Phys. Rev. B* **76**, 033101 (2007).
- ¹⁰⁴I. D. Prodan, G. E. Scuseria, and R. L. Martin, *Phys. Rev. B* **73**, 045104 (2006).
- ¹⁰⁵I. D. Prodan, J. A. Sordo, K. N. Kudin, G. E. Scuseria, and R. L. Martin, *J. Chem. Phys.* **123**, 014703 (2005).